Check for updates

ELECTROCHEMISTRY

Time-evolved hetero-alkali interphases enable long-life sulfide-based anode-free solid-state batteries

Jiwei Wang[1], Man Chen[2], Mengting Ye[1], Xiaolin Guo[2], Dehang Li[1], Hui Wang[2], Hongli Zhu[1]*

Copyright © 2026 The Authors, some rights reserved; exclusive licensee American Association for the Advancement of Science. No claim to original U.S. Government Works. Distributed under a Creative Commons Attribution NonCommercial License 4.0 (CC BY-NC).

Sulfide-based anode-free solid-state batteries (AFSSBs) offer high energy density and improved safety, but their practical implementation is hindered by parasitic reactions between freshly plated lithium (Li) and sulfide solid electrolytes. These reactions continuously consume the limited cathode-derived Li inventory, increase interfacial impedance, and promote nonuniform Li plating and stripping. Here, sodium bis(fluorosulfonyl)imide (NaFSI) is incorporated into $Li_{5.4}PS_{4.4}Cl_{1.6}$ (LPSC) to kinetically program interphase evolution. Heat treatment initially generates a NaF/LiF-rich interphase on the LPSC surface. This fluoride-rich region chemically stabilizes the interface and suppresses direct LPSC reduction. During the early cycles, the outermost region progressively evolves into a LiF/Li_3N-rich layer, while the NaF-containing phase becomes buried beneath the Li-rich surface region, producing a time-evolved compositional gradient. Although NaF provides effective chemical passivation, its poor Li^+ conductivity can impede interfacial ion transport. The subsequent formation of Li_3N-rich domains, which exhibit substantially higher Li^+ conductivity than NaF, provides more favorable transport pathways, homogenizes interfacial Li^+ flux, and promotes uniform Li plating and stripping. This time-evolved gradient interphase therefore combines early-stage chemical stabilization and Li conservation with improved long-term ion transport kinetics, suppressing impedance growth, localized inactive Li accumulation, and filamentary shorting. Consequently, the AFSSB using the NaFSI-modified LPSC interlayer retains 77.6% of its capacity after 500 cycles at 0.2 C, whereas the cell with bare LPSC retains only 32.1% after 100 cycles. These findings establish temporally programmed gradient interphases as a general strategy for conserving active Li and stabilizing sulfide-based AFSSBs.

INTRODUCTION

Sulfide-based anode-free solid-state batteries (AFSSBs) are emerging as a highly promising technology for achieving high energy density storage, as they eliminate the excess lithium (Li) metal anode and rely entirely on cathode-derived Li to form the anode during initial charging (*1*, *2*). This architectural simplification maximizes both gravimetric and volumetric energy density while offering inherent safety compared with liquid-based Li-metal batteries (*3*). However, despite their promise, sulfide-based AFSSBs remain far from practical implementation, largely because of persistent instability at the anode–solid electrolyte (SE) interface.

Unlike conventional Li metal batteries, anode-free batteries rely on in situ Li plating during initial charging, exposing freshly deposited Li directly to sulfide SEs. From a thermodynamic perspective, this direct contact drives continuous reductive decomposition of sulfide SEs to form a solid-electrolyte interphase (SEI) composed of resistive lithium sulfide (Li_2S), lithium chloride (LiCl), and lithium phosphide (Li_3P) phases, accelerates interfacial impedance growth, and ultimately causes severe capacity degradation (*4*–*6*). Simultaneously, the absence of a preloaded Li anode exacerbates Li nucleation heterogeneity, resulting in uneven Li plating and stripping and accelerated interfacial degradation (*7*). The uncontrolled Li deposition during cycling inevitably leads to the continuous accumulation of the resistive SEI, which accelerates the consumption of active Li inventory. These coupled chemo-electrochemical and morphological instabilities severely limit the long-term cycling of sulfide-based AFSSBs.

Considerable efforts have been devoted to mitigating interfacial degradation through carbon interlayers (*8*, *9*) and alloy engineering (*10*, *11*). While these approaches can improve interfacial stability, they often require complex processing steps and may compromise interfacial ion transport. In particular, carbon-based interlayers, while chemically stable against Li, typically suffer from intrinsically low Li^+ conductivity and dense microstructures, leading to sluggish Li^+ transport and unsatisfactory electrochemical performance at room temperature (*12*, *13*). These limitations underscore the inherent trade-off between chemical stability and ion transport efficiency in interlayer-based designs.

An alternative and potentially more scalable strategy is electrolyte chemistry regulation via additive engineering, which enables the in situ formation of a stable and ionically conductive SEI layer during cycling. In liquid electrolyte batteries, functional additives are widely used to form robust SEI layers in situ that effectively stabilize Li metal interfaces (*14*, *15*). Inspired by these advances, recent studies have shown that incorporating functional additives into sulfide SEs can induce the formation of robust protective SEI layers to stabilize Li metal anodes, without substantially compromising the intrinsic ionic conductivity of sulfide electrolytes (*16*–*18*). Moreover, compared with liquid systems, additive design principles for sulfide SEs remain largely unexplored, particularly in an anode-free configuration where freshly plated Li imposes more stringent interfacial stability requirements. Despite recent advances in interlayer designs (e.g., LiF-rich coatings, alloy interlayers, and metallic seeds), a key unresolved challenge in AFSSBs is the lack of interphases that can reproducibly reform during repeated exposure of freshly plated Li. Existing strategies largely assume a static passivation model, which is fundamentally incompatible with the anode-free architectures.

Here, we propose that interphases for anode-free batteries must be kinetically programmed, forming sequentially as cycling proceeds, to decouple early chemical passivation from efficient long-term Li^+

[1]Department of Mechanical and Industrial Engineering, Northeastern University, Boston, MA 02115, USA. [2]Mechanical Engineering Department, University of Louisville, Louisville, KY 40292, USA.
*Corresponding author. Email: h.zhu@neu.edu

Downloaded from https://www.science.org at Northeastern University on November 13, 2026

transport. Specifically, a simple yet effective interfacial regulation strategy by incorporating sodium bis(fluorosulfonyl)imide (NaFSI) molecular additives into $Li_{5.4}PS_{4.4}Cl_{1.6}$ (LPSC) SE for AFSSBs is investigated. NaFSI decomposes more readily than LiFSI because Na^+ provides weaker anion stabilization but a stronger thermodynamic pull toward NaF formation, lowering both kinetic and thermodynamic barriers for FSI^- decomposition. During cycling, Na-containing species are displaced, leading to the emergence of a LiF/Li_3N-dominated interphase. An early layer enriched with NaF/LiF forms initially at the electrolyte surface, while electrochemical cycling promotes the development of a LiF/Li_3N-rich layer. This sequential interphase formation decouples chemical stability and ionic transport, two competing requirements that cannot be simultaneously optimized in a single static interlayer. This dynamic interphase effectively suppresses LPSC reduction and resistive SEI formation, thereby stabilizing the anode/SE interphase during cycling. This work demonstrates a simple yet effective interface engineering strategy to stabilize the anode interface, providing valuable insights for developing long cycling high energy density sulfide-based AFSSBs.

RESULTS

Mechanistic principles of time-evolved interphase engineering for hetero-alkali SEI construction

The interfacial instability between LPSC and Li remains a central challenge for AFSSBs. As shown in Fig. 1A, LPSC readily reacts with initially plated Li, leading to the formation of a resistive SEI layer, containing Li_2S, LiCl, and Li_3P. This interphase hinders uniform Li^+ flux and progressively deteriorates during repeated plating/stripping processes, ultimately promoting localized Li accumulation and dendrite growth. To this end, a more robust and ionically conductive SEI is a key factor in stabilizing the AFSSBs. LiFSI-coated LPS has been demonstrated to induce LiF-rich interphase formation, thereby effectively stabilizing the Li metal anode (*19*). In liquid-based Li metal batteries, the introduction of Na-containing additives promotes the formation of hybrid SEI layers with enhanced mechanical robustness (*20*, *21*). In our design, we propose kinetically programmed SEI formation by introducing NaFSI as an interfacial additive to deliberately regulate chemical evolution in the interphase. As shown in Fig. 1B, the interfacial regulation enabled

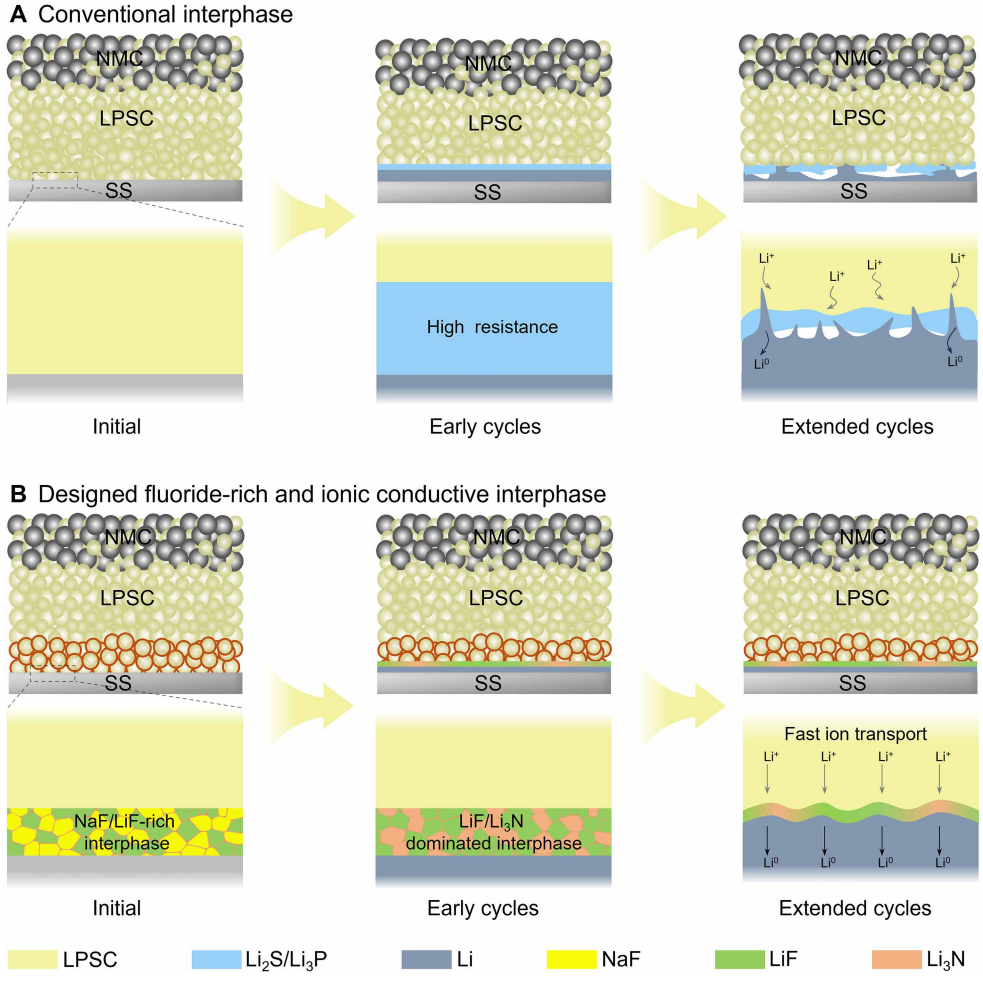


Fig. 1. Schematic illustration of anode interfacial evolution of AFSSBs. (**A**) Without and (**B**) with NaFSI@LPSC interlayer. Enlarged view of the anode interface in (A), showing the formation of a high-resistance interphase that hinders the Li^+ transport. Enlarged view of the anode interface in (B), illustrating a robust interphase with uniform Li^+ flux and fast and stable ion transport, enabling homogeneous Li deposition.

Downloaded from https://www.science.org at Northeastern University on November 13, 2026

by NaFSI follows a stepwise evolution process. During the synthesis process, NaFSI is likely to chemically interact with nucleophilic sulfide species on the LPSC surface, facilitating the cleavage of S-F bonds in the FSI^- anion and the release of F^-. The released F^- can be readily captured by Li^+ and Na^+ to form thermodynamically stable LiF/NaF (fig. S1A). Upon subsequent Li plating during the early cycles, further decomposition of FSI^- leads to the formation of a LiF/Li_3N-dominant SEI layer (fig. S1B) (*22*). Such a time-sequenced interphase evolution structure is expected to synergistically combine mechanical robustness with favorable Li^+ transport, thereby effectively homogenizing interfacial ion flux and enhancing resistance against interfacial degradation during repeated cycling.

The preparation procedures of the *x* wt% NaFSI@LPSC (denoted as *x*NF@LPSC) samples are schematically illustrated in Fig. 2A. Specifically, NaFSI and LPSC powders were thoroughly mixed in different weight ratios and subsequently pressed into a pellet. The pellet was then vacuum sealed and subjected to low-temperature thermal treatment (details are provided in the Materials and Methods). X-ray diffraction (XRD) patterns (Fig. 2B) reveal that all *x*NF@LPSC samples maintain the characteristic LPSC phase (space group $F\bar{4}3m$) without a secondary phase, indicating that the incorporation of NaFSI does not alter the bulk crystal structure of LPSC, although surface reaction may take place. Electrochemical impedance spectroscopy (EIS) measurements were conducted to evaluate the effect of NaFSI incorporation on the ionic conductivity of the *x*NF@LPSC composites (Fig. 2C). The pristine ball-milled LPSC exhibited a high ionic conductivity of 2.54 mS cm^{-1}, whereas the conductivity of the 3NF@LPSC decreased to 1.27 mS cm^{-1}. Further increasing the NaFSI content to 7NF@LPSC resulted in a pronounced reduction in conductivity to 0.52 mS cm^{-1}, suggesting that an excessive amount of NaFSI forms a thick coating layer on LPSC that impedes the Li-ion transport within SE (Fig. 2D). The conductivity reduction is attributed to the formation of a surface-confined fluoride-rich phase rather than bulk lattice disruption, as evidenced by unchanged XRD patterns.

Scanning electron microscopy (SEM) and corresponding energy-dispersive x-ray spectroscopy (EDS) element mapping images were used to investigate the morphology of the bare LPSC and *x*NF@LPSC, as well as the distribution of NaFSI on the LPSC particles. As shown in fig. S2, the introduction of NaFSI does not alter the morphology and particle size of the LPSC electrolyte. The EDS mapping results of 3NF@LPSC, with the S signals representative of the LPSC matrix, reveal a uniform distribution of F and Na signals on the surface of LPSC particles, indicating uniform distribution of NaFSI on the LPSC surface (Fig. 2, E to H). Similarly, the EDS mapping results of 5NF@LPSC and 7NF@LPSC also demonstrate the uniform distribution of NaFSI on the surface of LPSC particles (figs. S3 and S4).

Interfacial stability improvement with NF@LPSC interlayer

To evaluate the influence of the NaFSI additive on the interfacial stability, we measured the cell-level critical current density (cell-level CCD) of anode-free full cells with and without *x*NF@LPSC as the interlayer. The cell-level CCD test was conducted by cycling the AFSSBs at stepwise increased current densities starting from 0.1 mA

Downloaded from https://www.science.org at Northeastern University on November 13, 2026

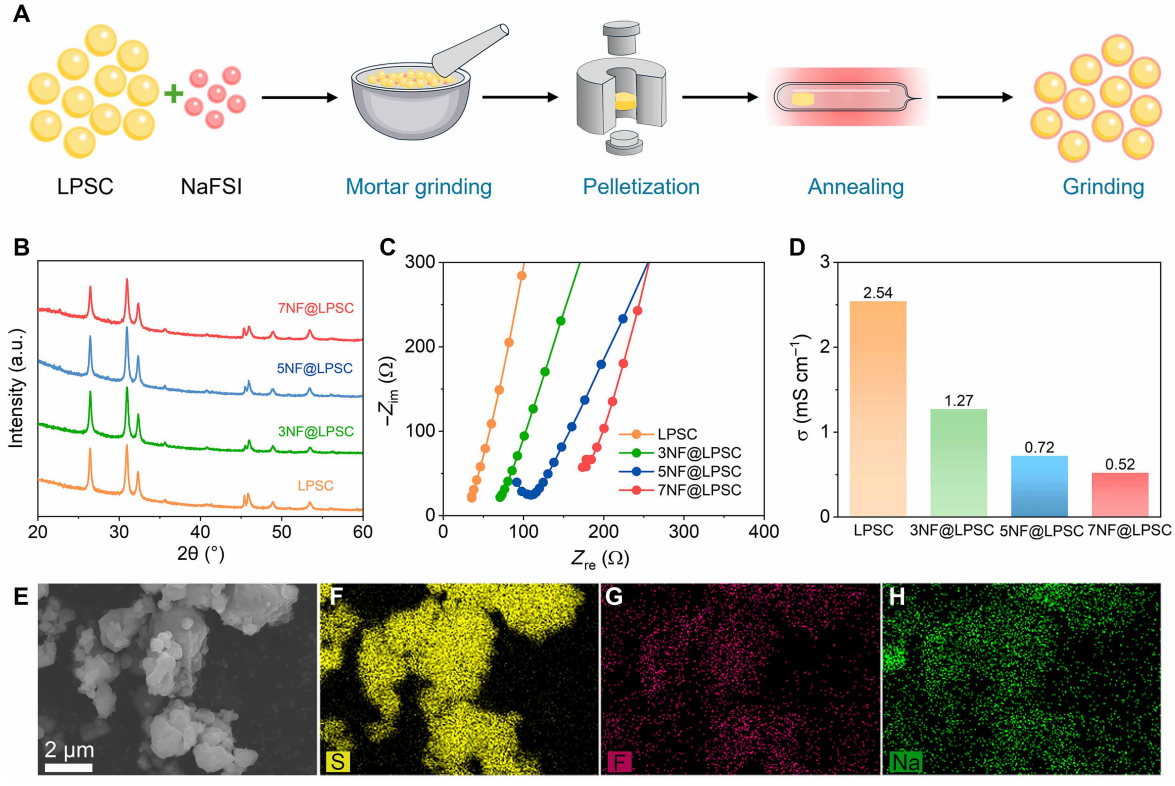


Fig. 2. Preparation and characterization of NaFSI@LPSC. (**A**) Schematic of the preparation procedures of the NaFSI@LPSC samples. (**B**) XRD patterns of the bare LPSC, 3NF@LPSC, 5NF@LPSC, and 7NF@LPSC. (**C**) Nyquist plots and (**D**) room temperature ionic conductivity of the bare LPSC, 3NF@LPSC, 5NF@LPSC, and 7NF@LPSC. (**E**) SEM image and (**F** to **H**) the corresponding EDS mapping of 3NF@LPSC.

cm^{-2} with an increasing step of 0.1 mA cm^{-2}. Here, the cell-level CCD is defined as the highest current density at which the full cell can operate without a short circuit or abnormal voltage behavior. Ag-coated stainless steel (Ag@SS) was used as the current collector to enhance lithiophilicity during cycling. When using bare LPSC as the SE and cycling with an 8.92 mg cm^{-2} active material mass loading, the cell-level CCD was found to be 0.9 mA cm^{-2} (Fig. 3A). The cell exhibits abnormal charging behavior during the Li plating process when the current density increased to 1.0 mA cm^{-2} (Fig. 3B and fig. S5), including a markedly increased charge capacity, distorted voltage profile, and a low Coulombic efficiency (CE). The abnormal increase in apparent charge capacity, together with voltage stagnation during charging and continued cell operation, is consistent with the electrochemical signatures of soft shorting reported in previous work (*23*, *24*), where internal current redistribution causes the measured capacity to deviate from the actual Faradaic Li-plating capacity. This behavior was even more severe in the following cycles. However, when using 3NF@LPSC as the interlayer, the cell-level CCD was increased to 1.5 mA cm^{-2} (Fig. 3C). The cell undergoes a soft short during the charge process as the current density increased to 1.6 mA cm^{-2}, in which overcharge took place and resulted in a low CE (Fig. 3D and fig. S6). The increased CCD value indicates that the introduction of 3NF@LPSC interlayer could improve the interfacial stability compared to that without the interlayer. Further increasing the NaFSI content in the interlayer results in a reduced cell-level CCD value (Fig. 3, E and F), which is because higher NaFSI content compromises the ionic conductivity and slows Li^+ transport within the interlayer, which will induce inhomogeneous Li deposition at increased current densities. Considering the ionic conductivity and interface stability improvement, 3NF@LPSC was chosen for subsequent electrochemical performance and mechanism studies.

Mechanism of 3NF@LPSC interlayer for stabilizing the interface

To unravel the interface stabilization mechanism of NaFSI-modified LPSC as the interlayer, surface-sensitive x-ray photoelectron spectroscopy

Downloaded from https://www.science.org at Northeastern University on November 13, 2026

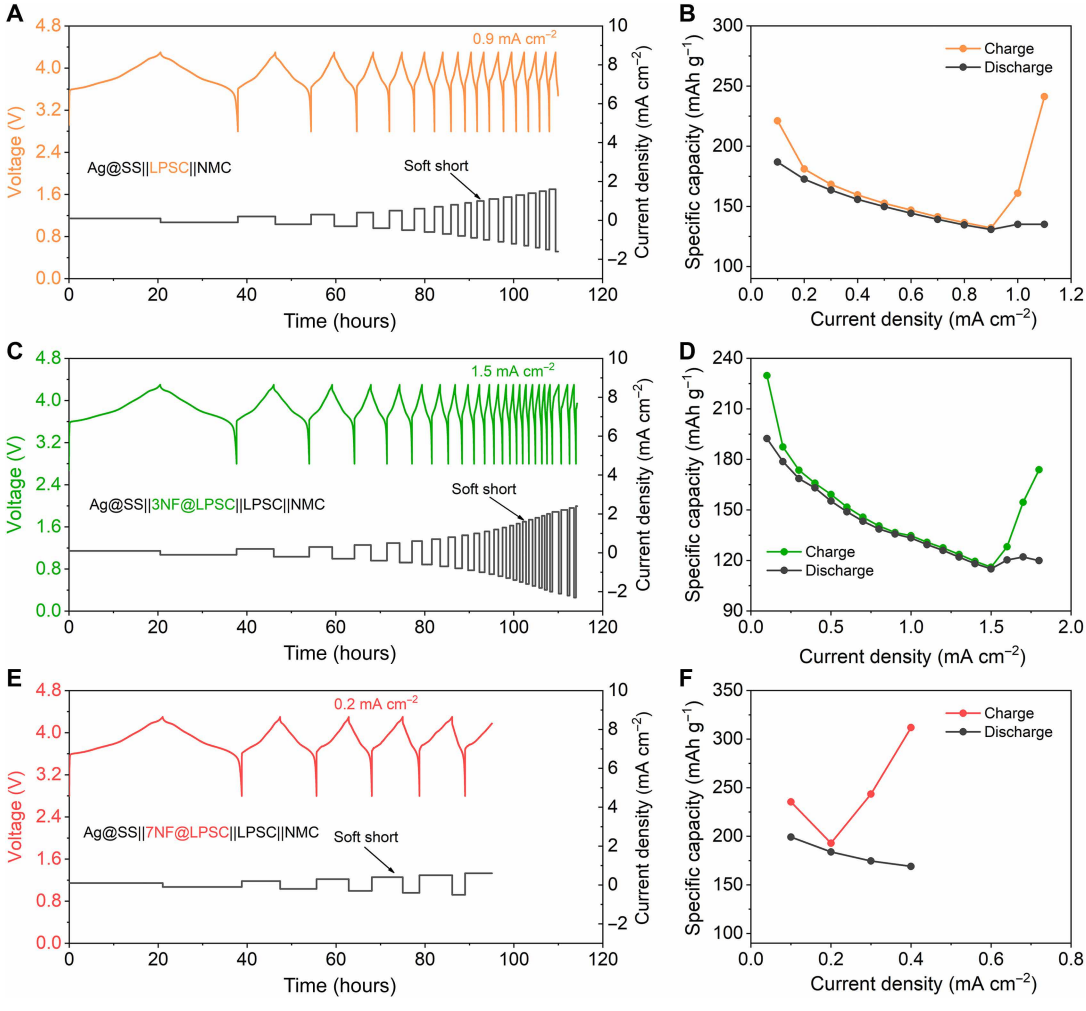


Fig. 3. Stepwise current tolerance tests of AFSSBs cycled using stepwise increased current densities starting from 0.1 mA cm^{-2} with an increasing step of 0.1 mA cm^{-2}. (**A**) Voltage profiles during the stepwise current tolerance test of the AFSSB with bare LPSC SE. (**B**) Specific charge/discharge capacities of the AFSSB with bare LPSC SE at different current densities. (**C**) Voltage profiles during the stepwise current tolerance test of the AFSSB with 3NF@LPSC interlayer. (**D**) Specific charge/discharge capacities of the AFSSB with 3NF@LPSC interlayer at different current densities. (**E**) Voltage profiles during the stepwise current tolerance test of the AFSSB with 7NF@LPSC interlayer. (**F**) Specific charge/discharge capacities of the AFSSB with 7NF@LPSC interlayer at different current densities.

(XPS) measurements were conducted for the pristine and cycled SE pellets facing the anode side to investigate the interface composition. Bare LPSC and NF@LPSC pellets before cycling were first examined. A survey scan of the 3NF@LPSC pellet shows obvious F and Na signals indicating the existence of NaFSI in the 3NF@LPSC, whereas neither F nor Na signals were observed in the survey scan of the bare LPSC (fig. S7). Figure 4A compares the S 2p spectra of different samples. For pure NaFSI, the S 2p spectrum is dominated by a characteristic doublet at 170 to 171 eV, which can be assigned to S (VI) species of -SO_2 moieties of the FSI^- anion (*25*). In contrast, bare LPSC exhibits a main S 2p doublet at 161.3 to 162.6 eV, corresponding to PS_4^{3-} tetrahedra of LPSC (*26*). Notably, the S 2p spectrum of 3NF@LPSC does not show obvious S (VI) species associated with intact FSI^- anions, in which the main peak is characterized by the PS_4^{3-} tetrahedra of LPSC, and a shoulder peak emerges at 163 to 165 eV, which is commonly attributed to S-S bonding or polysulfide-like species, suggesting interfacial reactions between LPSC and NaFSI (*27*). The interfacial decomposition of NaFSI is further supported by the F 1s spectra (Fig. 4B). The F 1s spectrum of NaFSI exhibits a main peak at 688.3 eV which can be assigned to -SO_2F species of NaFSI (*28*). In contrast, the F 1s spectrum of 3NF@LPSC exhibits a main peak centered at 685 eV, characteristic of inorganic fluoride species. A weak shoulder peak at 688 to 689 eV is also observed, which may originate from residual fluorinated fragments or unreacted NaFSI. The pronounced chemical shift directly confirms the transformation of fluorine from an anionic FSI^- environment to inorganic fluoride species. In addition, the Na 1s peak of 3NF@LPSC shifts toward lower binding energy compared with pristine NaFSI (Fig. 4C), indicating a more ionic chemical environment for Na and the formation of NaF (*29*). Furthermore, the presence of a strong inorganic fluorine signal together with surface-enriched Li suggests that Li participates in the formation of LiF at the interface (Fig. 4D). Thus, the XPS results demonstrate that the thermal treatment induces interfacial decomposition of FSI^- upon contact with LPSC,

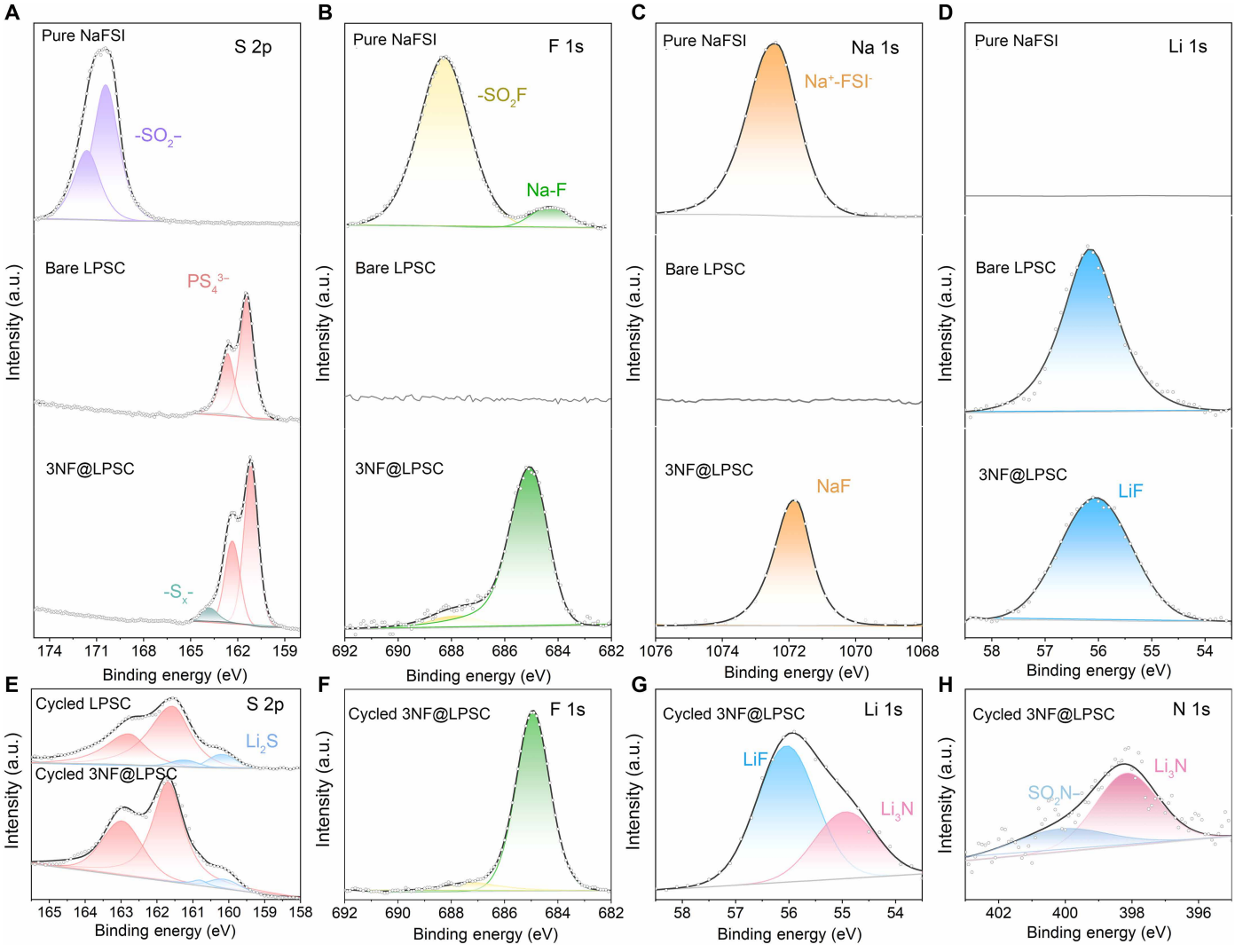


Fig. 4. Interphase chemistry of NaFSI-modified LPSC revealed by XPS. (**A**) S 2p, (**B**) F 1s, (**C**) Na 1s, and (**D**) Li 1s XPS spectra of pure NaFSI, bare LPSC, and 3NF@LPSC. (**E**) S 2p XPS spectra of cycled LPSC and 3NF@LPSC. (**F**) F 1s XPS spectrum of cycled 3NF@LPSC. (**G**) Li 1s spectrum of cycled 3NF@LPSC. (**H**) N 1s spectrum of cycled 3NF@LPSC.

Downloaded from https://www.science.org at Northeastern University on November 13, 2026

leading to the formation of an inorganic alkali-fluoride (LiF/NaF) interphase.

To elucidate the interfacial evolution during electrochemical cycling, XPS measurements were conducted on cycled LPSC and 3NF@LPSC. As shown in Fig. 4E, cycled LPSC exhibits a substantial weakening of the shoulder peak associated with the PS_4^{3-} at 162.7 eV. In addition, a distinct peak emerges at 160 eV, which can be assigned to Li_2S. These results indicate severe reductive decomposition at the interface. In contrast, the S 2p spectrum of cycled 3NF@LPSC remains dominated by a doublet peak associated with PS_4^{3-}, while Li_2S formation is reduced compared to cycled LPSC. Moreover, the cycled 3NF@LPSC shows an intensified inorganic F 1s signal at 684.9 eV, indicating further enrichment of the fluoride-rich interphase during cycling (Fig. 4F). Meanwhile, the Li 1s spectrum of cycled 3NF@LPSC reveals the emergence of an additional peak at a low binding energy (~54.5 to 55 eV) (Fig. 4G), suggesting nitrogen-containing inorganic products formed during cycling (*30*). This observation is consistent with the evolution of the N 1s spectra. Pure NaFSI displays a single N 1s peak centered at around 400.0 eV, characteristic of the SO_2N^- in the FSI^- anion (fig. S8). The N 1s spectrum of 3NF@LPSC before cycling is dominated by a broadened and slightly shifted peak at around 399.6 eV (fig. S9), indicating initial chemical interactions between NaFSI and the LPSC surface while the SO_2N^- in the FSI^- anion remains dominant. After cycling, the N 1s spectrum is dominated by a peak at 397 to 398 eV, accompanied by a diminished SO_2N^- contribution (Fig. 4H), suggesting the formation of Li_3N species during cycling (*17*, *30*). The Na 1s signal becomes very weak after cycling (fig. S10), implying that NaF species are no longer present within the surface-sensitive XPS probing depth. This attenuation is attributed to the growth of a Li-rich interphase, which dominates the surface region and masks Na species.

To investigate the dynamic evolution of the interphase formation during cycling, in-depth XPS measurements were performed after 1 cycle and 3 cycles. For both samples, the Na-F contribution in the F 1s spectra increases with sputtering depth, accompanied by a corresponding increase in the NaF signal in the Na 1s spectra (Fig. 5, A to D), indicating that NaF is retained within the interphase after cycling and is relatively enriched in the inner region of the interphase. Compared with the sample after 1 cycle, the residual -SO_2F signal is further reduced after 3 cycles, whereas the relative fraction of Na-F bonding in the F 1s spectra becomes higher. In contrast, the surface Na 1s intensity decreases slightly after 3 cycles. These observations suggest that NaFSI continues to decompose during the early cycles, while the newly formed NaF is gradually buried beneath the growing Li-rich surface layer rather than remaining at the outer surface. The surface N 1s, Li 1s, and S 2p spectra collected after the first cycle further identify the composition of the newly formed interphase (fig. S11). The appearance of a Li_3N-related N 1s component confirms that NaFSI decomposition produces nitrogen-containing inorganic species during the initial cycle, while the Li 1s spectrum indicates the concurrent formation of LiF. Moreover, no Li_2S-related peak is observed in the S 2p spectra, suggesting that the reductive decomposition of LPSC is effectively suppressed by the NaFSI-derived interphase.

The surface XPS spectra collected after different numbers of cycles provide further evidence for the temporal evolution of the interphase (Fig. 5, E to G). The surface Na signal gradually decreases with cycling and becomes nearly undetectable after 5 cycles, indicating that Na-containing species are progressively buried beneath the outer interphase. In contrast, the Li_3N-related N 1s component appears after the first cycle, remains detectable during subsequent cycling, and becomes more pronounced after 5 cycles. Although only limited changes are observed in the Li 1s spectra during the first few cycles, the emergence of the low binding energy peak after 5 cycles is consistent with the N 1s evolution, indicating the gradual development of Li_3N-related species within the outer interphase.

In summary, heat treatment initially generates a NaF/LiF-rich interphase on the LPSC surface. During the early cycles, the outermost region of this interphase progressively evolves into a LiF/Li_3N-rich layer, while the NaF-containing phase becomes buried beneath the Li-rich surface layer. The initial NaF/LiF-rich interphase suppresses early-stage LPSC reduction and provides chemical stabilization; however, NaF is a poor Li^+ conductor and limits interfacial ion transport. The subsequent formation of Li_3N, which exhibits substantially higher Li^+ conductivity than NaF, facilitates faster and more homogeneous Li^+ transport across the interface. This time-evolved gradient interphase therefore combines early-stage chemical passivation with improved long-term ion transport kinetics, ultimately promoting more uniform Li plating and stripping.

Electrochemical performance of AFSSBs with 3NF@LPSC interlayer

To validate the practical viability of the 3NF@LPSC interlayer, anode-free full cells were tested with $LiNbO_3$-coated $LiNi_{0.82}Mn_{0.07}Co_{0.11}O_2$ (NMC) as the cathode. A 10-mg 3NF@LPSC interlayer was introduced between the current collector and 70- to 75-mg LPSC SE. Figure 6A shows the cycling performance of the Ag@SS||LPSC||NMC and Ag@SS||3NF@LPSC||LPSC||NMC AFSSBs at 0.1 C with an active material mass loading of 8.92 mg cm^{-2}. The two cells exhibit comparable initial charge/discharge capacities (fig. S12A), with initial Coulombic efficiencies of 80.6 and 80.1%, respectively. However, the incorporation of the 3NF@LPSC interlayer leads to markedly enhanced cycling stability. The cell with 3NF@LPSC retains a discharge capacity of 153.4 mAh g^{-1} after 100 cycles (fig. S12B), exhibiting a superior capacity retention of 89%. In contrast, the cell without the interlayer exhibits accelerated capacity decay, only delivering a discharge capacity of 108.2 mAh g^{-1} after 100 cycles (fig. S12B), corresponding to a capacity retention of 62.3%. The cycling performance of the SS||LPSC||NMC cell was also evaluated under the same conditions (fig. S13) to elucidate the role of Ag in promoting the uniform plating/stripping. Without Ag, the SS||LPSC||NMC cell displays rapid capacity decay, with a discharge capacity of 76.8 mAh g^{-1} after 100 cycles (fig. S14), which is much lower than that of the cell with Ag. These results suggest the effectiveness of Ag and 3NF@LPSC in promoting stable Li plating/stripping and suppressing interfacial reactions in AFSSBs.

Rate capability comparison was further carried out to unveil the interface stability of 3NF@LPSC. Figure S15 presents the rate performance of AFSSBs with/without 3NF@LPSC at an active material mass loading of 8.92 mg cm^{-2}. The cells underwent 5 cycles at each rate from 0.1 C to 1 C, followed by a recovery to 0.1 C. Figure S16 shows the galvanostatic charge/discharge voltage profiles at each rate. Although both cells show similar charge/discharge capacities at low rates of 0.1 C and 0.2 C, the cell without 3NF@LPSC exhibits a sharp voltage drop near the end of the discharge at 0.3 C, indicating interface contact failure at the end of Li stripping. This interface contact failure is further accelerated at 0.5 C as indicated by the light

Downloaded from https://www.science.org at Northeastern University on November 13, 2026

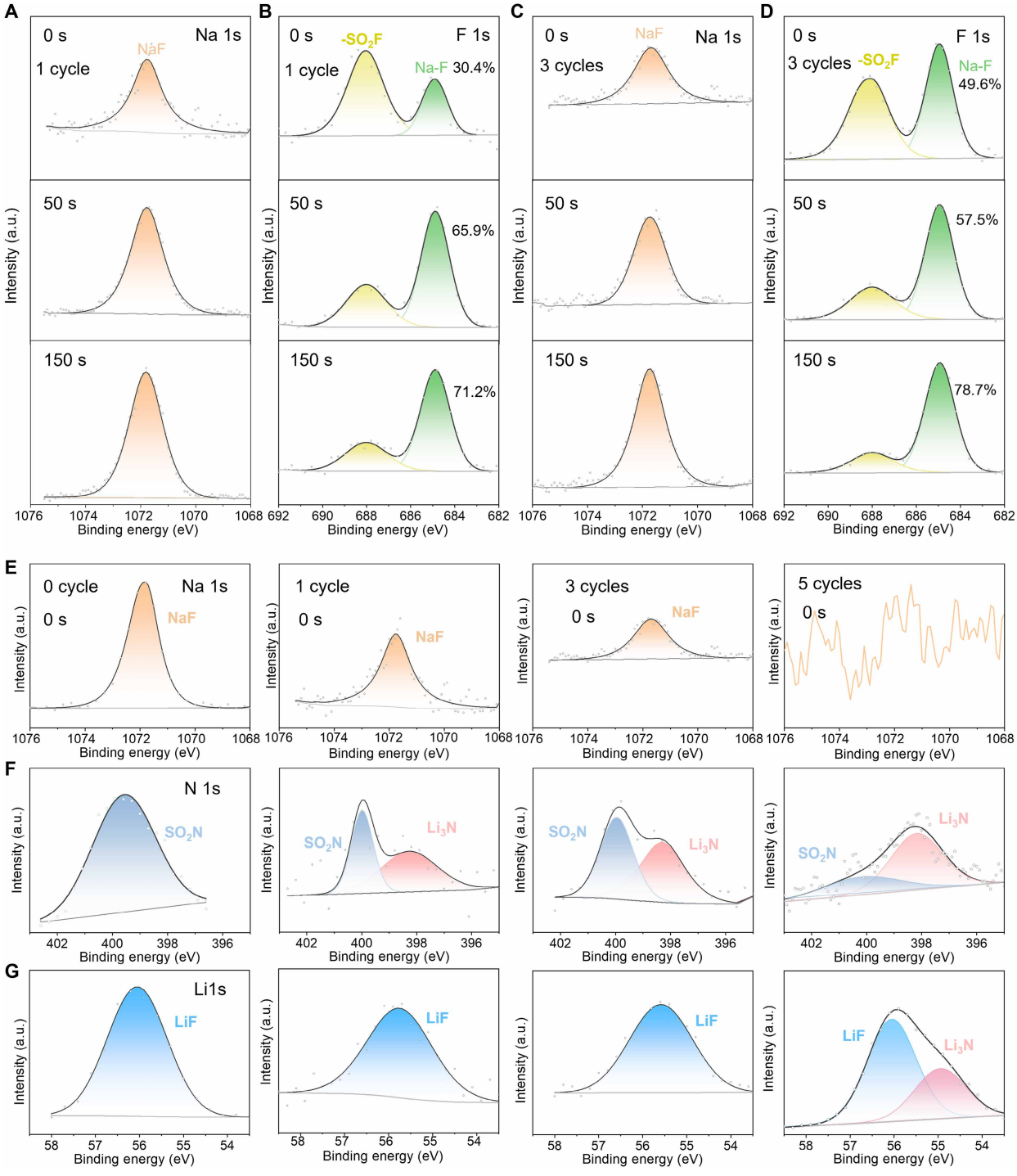


Fig. 5. Depth-dependent and cycling-dependent evolution of the hetero-alkali interphase. XPS depth spectra of cycled 3NF@LPSC at different sputtering times. (**A**) Na 1s and (**B**) F 1s after 1 cycle. (**C**) Na 1s and (**D**) F 1s after 3 cycles. (**E** to **G**) The surface XPS spectra of Na 1s, N 1s, and Li 1s before cycling (0 cycles) and after 1, 3, and 5 cycles.

green arrow in fig. S16A. The cell short circuits at 1 C. By contrast, the cell with 3NF@LPSC displays stable cycling from 0.1 C to 0.5 C, suggesting robust interface contact (fig. S16B). However, the cell still undergoes a soft short when the C rate is increased to 1 C because the current density at 1 C is 1.78 mA cm^{-2} and exceeds its cell-level CCD value. Rate capability was further compared with a lower active material mass loading of 6.24 mg cm^{-2} using the identical cycling protocol. Figure 6 (B and C) displays the galvanostatic charge/discharge profiles of the two cells at each rate. The cell with 3NF@LPSC demonstrates superior rate capability up to 1 C without short-circuiting, delivering discharge capacities of 176.2, 152.6, 137.5, 118.6, and 89 mAh g^{-1} at 0.1 C, 0.2 C, 0.3 C, 0.5 C, and 1 C,

Downloaded from https://www.science.org at Northeastern University on November 13, 2026

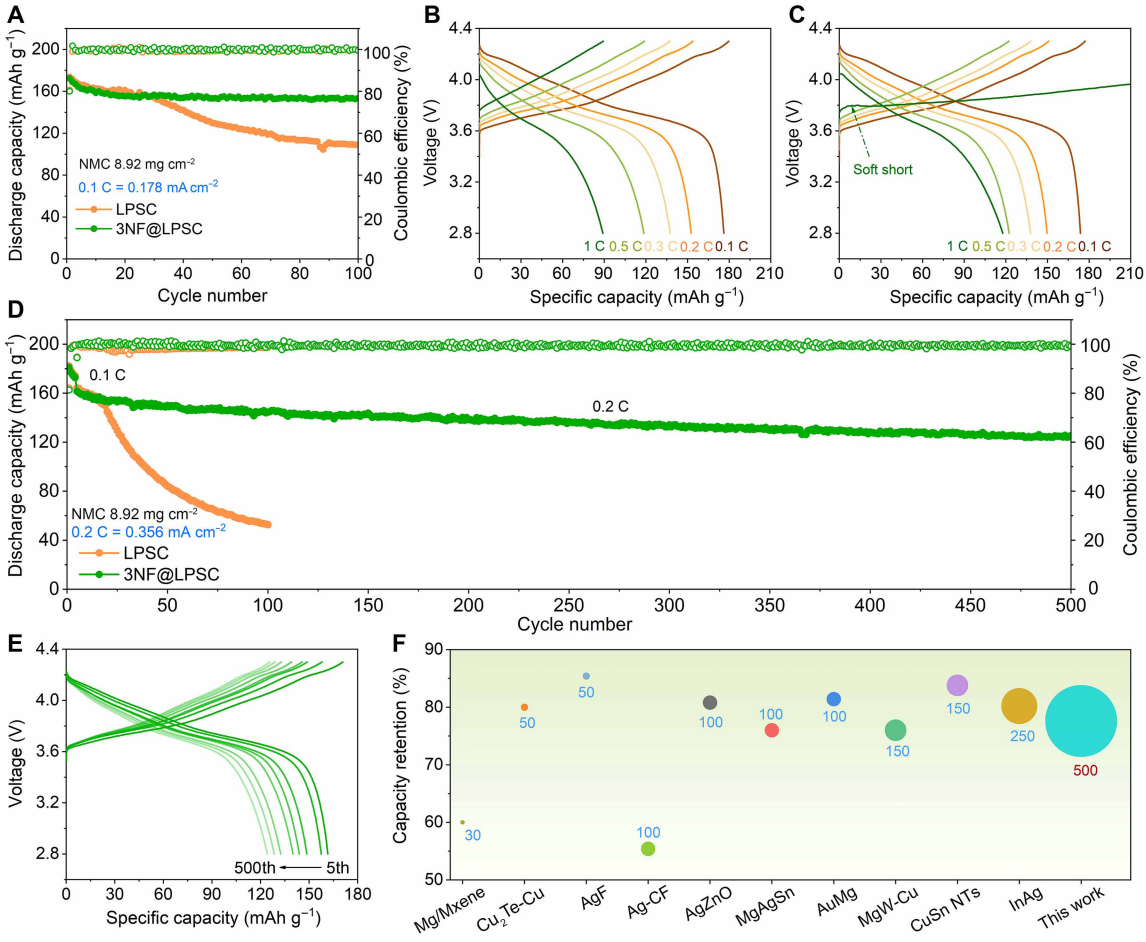


Fig. 6. Electrochemical performance of AFSSBs with the 3NF@LPSC interlayer. (**A**) Long-term cycling performance of AFSSBs with and without the 3NF@LPSC interlayer at 0.1 C. (**B** and **C**) Rate capability of AFSSBs with and without the 3NF@LPSC interlayer. (**D**) Long-term cycling performance of AFSSBs at 0.2 C. (**E**) Representative charge-discharge voltage profiles of AFSSBs with the 3NF@LPSC interlayer from the 5th to the 500th cycle. (**F**) Comparison of the full cell performance of reported AFSSBs with LPSC SEs.

respectively (Fig. 6B). In particular, the discharge capacity recovers to the original level when the current rate returns to 0.1 C, implying great interfacial stability (fig. S17). In contrast, the cell without 3NF@LPSC short-circuits at 1 C even with the cathode mass loading reduced, leading to overcharging and lower CE in subsequent cycles (Fig. 6C).

Long-term cycling performance was further evaluated at 0.2 C to validate the interface stability enhancement due to the existence of 3NF@LPSC interlayer. Figure 6D compares cycling performance of the two anode-free cells with/without 3NF@LPSC. Both cells underwent an activation cycling process at 0.1 C for 4 cycles and then switched to 0.2 C (equivalent to 0.356 mA cm^{-2}) for long-term cycling. The two cells show similar trends of capacity decrease during the four activation cycles. Upon switching to 0.2 C, the two cells deliver initial discharge capacities of 164.3 and 161.6 mAh g^{-1}. However, the cell without 3NF@LPSC shows an interfacial contact issue at the end of the stripping process at the 20th cycle and exhibits accelerated capacity decay in the subsequent cycles. As a result, it only retains a discharge capacity of 52.7 mAh g^{-1} after 100 cycles (fig. S18), yielding a capacity retention of 32.1%. In contrast, the cell with 3NF@LPSC presents exceptional cycling stability over 500 cycles, maintaining a discharge capacity of 125.4 mAh g^{-1} (Fig. 6E), corresponding to a retention rate of 77.6%, with a decay rate of 0.045% per cycle. Moreover, the cell with 3NF@LPSC shows an average CE of ~99.64% throughout 500 cycles, indicating highly reversible Li plating/stripping during repeated cycling, whereas the cell without 3NF@LPSC only achieves an average CE of 98.30% over 100 cycles, further demonstrating the effectiveness of the dynamic hetero-alkali interphase in stabilizing the anode-free battery during prolonged cycling. Furthermore, the electrochemical performance using 3LiFSI@LPSC (3LF@LPSC) interlayer was evaluated in an AFSSB using the same Ag@SS current collector and NMC mass loading. As shown in figs. S19 and S20, although the 3LF@LPSC slightly improves cycling stability compared with the cell without an interlayer, the cell still experiences interfacial contact loss after the 27th cycle, followed by a fast capacity decay. These results highlight the superior interfacial stabilization capability of the 3NF@LPSC-derived dynamic hetero-alkali interphase. As summarized in Fig. 6F, the electrochemical performance with the 3NF@LPSC interlayer shows promise under practical cycling conditions compared to previous sulfide-based AFSSB studies with state-of-the-art performance (*24*, *31*–*39*). To evaluate the effectiveness of the 3NF@LPSC interlayer under

Downloaded from https://www.science.org at Northeastern University on November 13, 2026

reduced stack pressure, the electrochemical performance of AFSSBs was further investigated at 5 MPa. As shown in fig. S21, both cells exhibit inferior cycling stability compared with those cycled at 15 MPa. The cell without the 3NF@LPSC interlayer exhibits interfacial contact loss as early as the 8th cycle, whereas the onset of interfacial contact loss is delayed to the 20th cycle in the cell with the 3NF@LPSC interlayer. These results indicate that the NaFSI-derived interphase effectively delays interfacial degradation and prolongs the cycling stability of anode-free solid-state batteries under reduced stack pressure. However, achieving long-term cycling stability at low stack pressure remains challenging and requires further optimization of both interphase and cell engineering strategies.

Cross-sectional SEM was used to investigate the postcycling deposited Li morphology in AFSSBs with and without 3NF@LPSC interlayer. Both cells were cycled five times to 100% state of charge at 0.1 C. As shown in fig. S22, the deposited Li is located between the LPSC SE and the Ag@SS current collector, as indicated by the pink dashed lines. The corresponding EDS further confirms the location of each component. The Fe signal originates from the SS current collector, while the O signal is associated with the deposited Li. Weak P, S, and Cl signals indicate that a small amount of LPSC particles remains attached to the Li layer. In the cell without 3NF@LPSC interlayer (fig. S22A), the deposited Li exhibits a relatively loose morphology. The enlarged SEM image (fig. S23) reveals that the deposited Li is composed of loosely packed flake-like features with microscale voids distributed throughout the deposited Li layer, suggesting poor compactness of the deposited Li layer. Moreover, the deposited Li at another location exhibits a similar morphology but a substantially smaller thickness (fig. S24), indicating nonuniform Li deposition in the cell without 3NF@LPSC interlayer. This nonuniform deposition is likely associated with the continuous formation of high-resistance Li_2S interphase species during cycling, which leads to nonuniform Li^+ flux across the interface and consequently uneven Li deposition. In contrast, the deposited Li in the cell with 3NF@LPSC forms a much denser and more continuous Li layer without obvious flake-like features (fig. S22B), and a low-magnification SEM image (fig. S25) further confirms the uniformity of the deposited Li over a wide area, suggesting that the NaFSI-derived interphase effectively promotes compact and homogeneous Li deposition.

In situ EIS and distribution of relaxation times (DRT) analysis were further performed to investigate the interfacial resistance evolution of AFSSBs with and without the 3NF@LPSC interlayer at different cycles. In situ EIS spectra and DRT contour maps show that both cells exhibit similar interfacial resistance in the initial cycle at 0.1 C (Fig. 7, A to F), suggesting similar initial interfacial contact and reaction kinetics. However, at the 10th cycle at 0.2 C, the cell without the 3NF@LPSC interlayer shows a pronounced increase in interfacial impedance as evidenced by the enlarged semicircle in the EIS spectra, particularly near the end of the stripping (Fig. 7, G and H). The corresponding DRT results provide further insights into the origin of the impedance growth. In the DRT contour maps, R1 shows an obvious intensity increase near the end of stripping, indicating poor interfacial contact. Meanwhile, the enhanced R2 signal suggests an increased resistance of the SEI layer, resulting from the undesirable side reactions between Li and LPSC. In addition, the increased charge transfer resistance (R4) reflects sluggish interfacial kinetics associated with progressive interfacial degradation. In contrast, the cell with 3NF@LPSC exhibits markedly weaker DRT peak intensities in the R1, R2, and R4 regions at the 10th cycle at 0.2 C (Fig. 7, J to L), indicating stabilized interfacial contact and suppressed interfacial side reactions. Furthermore, at the 20th cycle, the cell without the interlayer shows a further intensified R1 signal near the end of stripping in the DRT contour map, implying continued interfacial deterioration, whereas the cell with the 3NF@LPSC interlayer maintains stable interface contact and SEI resistance (fig. S26). These results demonstrate that the 3NF@LPSC interlayer effectively suppresses interfacial side reactions, stabilizes the anode/electrolyte interface, and reduces SEI-related resistance, which provide complementary electrochemical evidence, consistent with the XPS results, explaining the enhanced cycling stability of the anode-free cells enabled by the 3NF@LPSC interlayer. The suppressed growth of R1, R2, and R4 components indicates that the dynamic interphase stabilizes both physical contact and interfacial chemistry during repeated Li stripping, a failure mode unique to anode-free architectures.

DISCUSSION

In summary, incorporating NaFSI into LPSC creates a time-evolved gradient interphase that simultaneously limits irreversible Li loss and improves interfacial Li^+ transport in sulfide-based AFSSBs. Heat treatment initially generates a NaF/LiF-rich interphase on the LPSC surface. This chemically stable fluoride-rich region suppresses direct reduction of LPSC and inhibits the continued formation and accumulation of resistive decomposition-derived SEI products, thereby limiting the ongoing consumption of the finite cathode-derived Li inventory. During the early cycles, the outermost region of the interphase progressively evolves into a LiF/Li_3N-rich layer, while the NaF-containing phase becomes buried beneath the Li-rich surface region. This spatial and temporal differentiation enables the interphase to perform complementary functions. The NaF/LiF-containing region provides chemical passivation and suppresses parasitic Li consumption, whereas the emergence of Li_3N-rich domains in the outer layer alleviates the ion transport limitation associated with poorly Li^+-conductive NaF. Because Li_3N exhibits substantially higher Li^+ conductivity than NaF, its formation facilitates faster and more homogeneous Li^+ transport across the interface, homogenizes interfacial Li^+ flux, and promotes dense and uniform Li plating and stripping. This mechanism is supported by the complementary characterization results. XPS reveals the progressive evolution from an initial NaF/LiF-rich interphase to a gradient structure containing a LiF/Li_3N-rich outer region and a buried NaF-containing region, together with suppressed LPSC decomposition. EIS and DRT analyses demonstrate reduced growth of SEI-related, interfacial contact, and charge transfer resistances, while cross-sectional SEM confirms denser and more homogeneous Li deposition. Consequently, the AFSSB using the 3NF@LPSC interlayer maintains a discharge capacity of 125.4 mAh g^{-1} after 500 cycles at 0.2 C, corresponding to 77.6% capacity retention. In contrast, the cell using bare LPSC retains only 52.7 mAh g^{-1} after 100 cycles, corresponding to 32.1% capacity retention. This temporal separation of chemical stabilization and ion transport provides a dynamic design principle for conserving active Li and extending the lifetime of anode-free solid-state batteries.

MATERIALS AND METHODS

Synthesis of fine $Li_{5.4}PS_{4.4}Cl_{1.6}$ (LPSC)

$Li_{5.4}PS_{4.4}Cl_{1.6}$ (LPSC) was synthesized via a mechanical ball-milling process followed by annealing (*40*). Specifically, lithium sulfide

Downloaded from https://www.science.org at Northeastern University on November 13, 2026

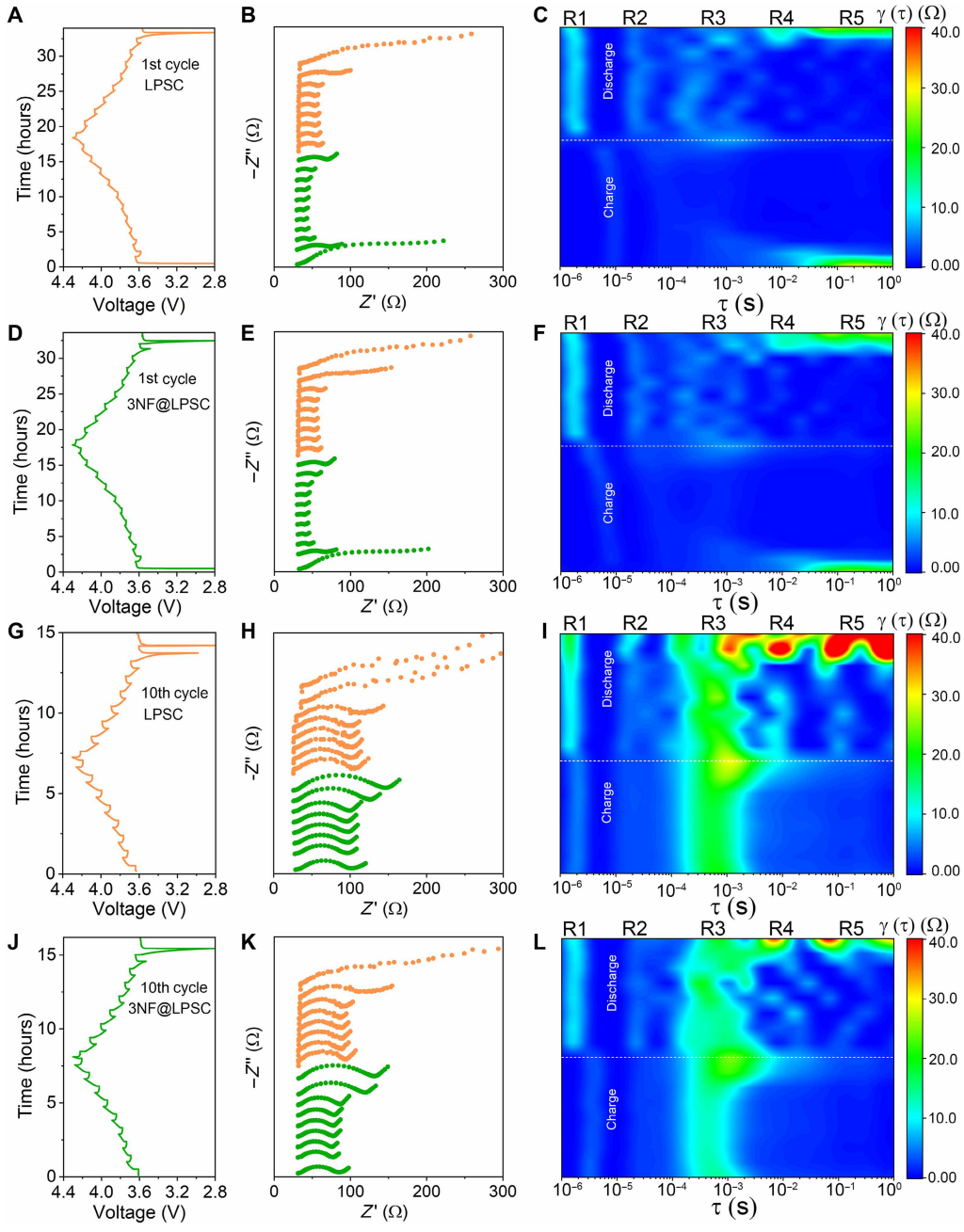


Fig. 7. Interfacial resistance evolution of AFSSBs revealed by in situ EIS and DRT. Charge-discharge profiles of cells (**A** and **G**) without and (**D** and **J**) with 3NF@LPSC interlayer at the 1st and 10th cycles in the EIS measurements. The 1st cycle was tested at 0.1 C, and the 10th cycle was tested at 0.2 C. In situ EIS plots of cells (**B** and **H**) without and (**E** and **K**) with 3NF@LPSC interlayer at the 1st and 10th cycles. DRT contour plots of cells (**C** and **I**) without and (**F** and **L**) with 3NF@LPSC interlayer at the 1st and 10th cycles.

(Li_2S, 99.98%, Sigma-Aldrich), phosphorus pentasulfide (P_2S_5, 99%, Sigma-Aldrich), and LiCl (>99.98%, Sigma-Aldrich) were stoichiometrically mixed manually in an agate mortar, and the mixed powders were then transferred into a stainless steel (SS) jar in an Ar glove box and ball-milled at 500 rpm for 40 cycles, with each cycle consisting of 15-min milling followed by a 15-min rest. After ball milling, the mixture was sealed in a glass tube under vacuum and annealed at 510°C for 2 hours with a heating rate of 5°C/min. To obtain fine LPSC, the as-prepared LPSC SE was subjected to a secondary ball-milling step. Specifically, 2 g of LPSC was placed into a zirconia jar and sealed inside the glove box. Ball milling was then conducted at a speed of 300 rpm for 13 hours, using a cycle of 20-min milling and 5-min rest.

Preparation of *x*NaFSI-LPSC (*x* = 3, 5, and 7)

For the preparation of *x*NaFSI-LPSC (denoted as *x*NF@LPSC), the fine LPSC and NaFSI powders were first mechanically mixed in an

Downloaded from https://www.science.org at Northeastern University on November 13, 2026

agate mortar for 20 min with different mass ratios of 3:100, 5:100, and 7:100, which were denoted as 3NF@LPSC, 5NF@LPSC, and 7NF@LPSC. Afterward, the mixture was compressed into a pellet with a pressure of 200 MPa. The pellet was vacuum sealed into a glass tube and annealed at 130°C for 1 hour with a heating rate of 1°C/min, followed by cooling down to room temperature with a cooling rate of 1°C/min. After cooling down, the *x*NF@LPSC powders were obtained by hand-grinding the pellets in a mortar. For comparison, 3LiFSI-LPSC (noted as 3LF@LPSC) was prepared using the same procedure as 3NF@LPSC, except that the pellet was annealed at 260°C for 1 hour.

Conductivity measurements

The ionic conductivity of the *x*NF@LPSC samples was measured by EIS. Samples (90 to 100 mg) were cold pressed into pellets in polyether ether ketone (PEEK) cells with a diameter of 10 mm under a pressure of 350 MPa, and two SS plungers served as ionic blocking electrodes. EIS was performed using a Biologic SP 150 potentiostat in the frequency range between 1000 mHz and 1 MHz with an amplitude of 20 mV.

Anode-free cell fabrication

The composite cathode was prepared by hand mixing $LiNbO_3$-coated $LiNi_{0.82}Mn_{0.07}Co_{0.11}O_2$ cathode (MSE Supplies), fine LPSC, and vapor-grown carbon fibers in a weight ratio of 70:28.5:1.5. For anode-free full cells with an interlayer, 70 to 75 mg of fine LPSC powders was first poured into a PEEK cell with a diameter of 10 mm and compressed into a pellet at a low pressure of 40 MPa, and then 10 mg of *x*NF@LPSC ($x = 3$, 5, and 7) or 3LF@LPSC powders was loaded on one side of the SE pellet, followed by compressing under a low pressure. Then, 10 mg of cathode composites was evenly spread on the other side of the SE pellet and compressed with a 10-mm-diameter steel pillar by hand. For the anode-free full cells without an interlayer, a total of 80 to 85 mg of fine LPSC powders was used as the SE pellet. The other procedures were the same as those for the cells with an interlayer. The cell stack was then pressed at a high pressure of 375 MPa for 1 min to densify all the layers. Afterward, a 10-mm-diameter disc metal foil (100-nm Ag-coated SS) was placed on the anode side of the SE pellet. The cell was then positioned in an SS frame, and an external pressure of 5 or 15 MPa was applied by using a torque wrench during the cell testing.

Electrochemical characterization

Electrochemical cycling measurements were conducted inside the Ar-filled glove box to avoid air exposure. The electrochemical performance of the anode-free full cells was tested within the voltage range of 2.8 to 4.3 V versus Li^+/Li. Operando EIS measurement was carried out over a frequency range from 1 MHz to 10 mHz with an ac amplitude of 20 mV using a Biologic SP 150 potentiostat. Cells were galvanostatically cycled at 0.1 C for the 1st cycle and at 0.2 C for the 10th and 20th cycles. EIS spectra were collected every 1-hour charge or discharge followed by 30-min rest and at the end of charge or discharge for the first cycle. For 10th and 20th cycles, EIS spectra were collected every 30 min charge or discharge followed by 15-min rest and at the end of charge or discharge. All the electrochemical measurements were performed on a Landt battery cycler or a Bio-Logic cycler. All electrochemical measurements were conducted at room temperature (25°C).

Material characterizations

The SEM images and EDS spectra were acquired with a Hitachi S4800 scanning electron microscope set at 10 kV. XRD measurements were conducted with a Bruker D8 Discover diffractometer (nickel-filtered Cu Kα radiation, $\lambda = 1.5418$ Å) to verify the phase purity of the as-prepared *x*NF@LPSC ($x = 0$, 3, 5, and 7) powders. XPS with Al Kα x-ray radiation was used to reveal the surface chemical compositions of the SE pellets before and after cycling.

Supplementary Materials

This PDF file includes:

Figs. S1 to S26

REFERENCES

1. S. E. Sandoval, C. G. Haslam, B. S. Vishnugopi, D. W. Liao, J. S. Yoon, S. H. Park, Y. Wang, D. Mitlin, K. B. Hatzell, D. J. Siegel, P. P. Mukherjee, N. P. Dasgupta, J. Sakamoto, M. T. McDowell, Electro-chemo-mechanics of anode-free solid-state batteries. *Nat. Mater.* **24**, 673–681 (2025).
2. J. Wang, H. Zhu, Sulfide-based anode-free solid-state batteries: Key challenges and emerging solutions. *ACS Energy Lett.* **10**, 2377–2391 (2025).
3. W. Z. Huang, C. Z. Zhao, P. Wu, H. Yuan, W. E. Feng, Z. Y. Liu, Y. Lu, S. Sun, Z. H. Fu, J. K. Hu, S. J. Yang, J. Q. Huang, Q. Zhang, Anode-free solid-state lithium batteries: A review. *Adv. Energy Mater.* **12**, 2201044 (2022).
4. J. Wang, Y. Liu, M. Ye, G. Wang, C. Xu, H. Zhu, Fundamental understanding of "fresh" lithium nucleation and growth in sulfide-based anode-free solid-state batteries: Effects of substrate, current density, and Li^+ supply. *Small* **21**, e06473 (2025).
5. A. L. Davis, E. Kazyak, D. W. Liao, K. N. Wood, N. P. Dasgupta, Operando analysis of interphase dynamics in anode-free solid-state batteries with sulfide electrolytes. *J. Electrochem. Soc.* **168**, 070557 (2021).
6. H. Wan, Z. Wang, W. Zhang, X. He, C. Wang, Interface design for all-solid-state lithium batteries. *Nature* **623**, 739–744 (2023).
7. J.-A. Lee, H. Kang, S. Kim, K. Lee, J. H. Byun, E. Kwon, S. Seo, K. Kwak, K. H. Ryu, N.-S. Choi, Unveiling degradation mechanisms of anode-free Li-metal batteries. *Energy Storage Mater.* **73**, 103826 (2024).
8. Y.-G. Lee, S. Fujiki, C. Jung, N. Suzuki, N. Yashiro, R. Omoda, D.-S. Ko, T. Shiratsuchi, T. Sugimoto, S. Ryu, J. H. Ku, T. Watanabe, Y. Park, Y. Aihara, D. Im, I. T. Han, High-energy long-cycling all-solid-state lithium metal batteries enabled by silver–carbon composite anodes. *Nat. Energy* **5**, 299–308 (2020).
9. D. Spencer-Jolly, V. Agarwal, C. Doerrer, B. Hu, S. Zhang, D. L. R. Melvin, H. Gao, X. Gao, P. Adamson, O. V. Magdysyuk, P. S. Grant, R. A. House, P. G. Bruce, Structural changes in the silver-carbon composite anode interlayer of solid-state batteries. *Joule* **7**, 503–514 (2023).
10. S. E. Sandoval, J. A. Lewis, B. S. Vishnugopi, D. L. Nelson, M. M. Schneider, F. J. Q. Cortes, C. M. Matthews, J. Watt, M. Tian, P. Shevchenko, P. P. Mukherjee, M. T. McDowell, Structural and electrochemical evolution of alloy interfacial layers in anode-free solid-state batteries. *Joule* **7**, 2054–2073 (2023).
11. J. Oh, S. H. Choi, H. Kim, J. Y. Kim, G.-J. Lee, K. Y. Bae, T. Lee, N. Lee, Y. Sohn, W. J. Chung, J. W. Choi, Lithio-amphiphilic nanobilayer for high energy density anode-less all-solid-state batteries operating under low stack pressure. *Energy Environ. Sci.* **17**, 7932–7943 (2024).
12. N. Suzuki, N. Yashiro, S. Fujiki, R. Omoda, T. Shiratsuchi, T. Watanabe, Y. Aihara, Highly cyclable all-solid-state battery with deposition-type lithium metal anode based on thin carbon black layer. *Adv. Energy Sustain. Res.* **2**, 2100066 (2021).
13. D. W. Liao, T. H. Cho, S. Sarna, M. K. Jangid, H. Kawakami, T. Kotaka, K. Aotani, N. P. Dasgupta, Interfacial dynamics of carbon interlayers in anode-free solid-state batteries. *J. Mater. Chem. A* **12**, 5990–6003 (2024).
14. J. Liu, W. Hao, M. Fang, X. Chen, Y. Dong, Y. Chen, Z. Wang, X. Yue, Z. Liang, Screening of F-containing electrolyte additives and clarifying their decomposition routes for stable Li metal anodes. *Nat. Commun.* **15**, 9356 (2024).
15. S. Yuan, T. Kong, Y. Zhang, P. Dong, Y. Zhang, X. Dong, Y. Wang, Y. Xia, Advanced electrolyte design for high-energy-density Li-metal batteries under practical conditions. *Angew. Chem. Int. Ed. Engl.* **60**, 25624–25638 (2021).
16. Z. He, Y. Liu, Y. Liu, H. Xiao, Z. Xie, C. Sheng, A. Chen, P. He, H. Zhou, Hybrid coating on sulfide electrolytes via lithium salts additive for stable all-solid-state lithium metal batteries. *ACS Nano* **19**, 33523–33533 (2025).
17. S. Zhang, Q. Li, J. Gao, R. Liu, X. Jiang, S. Xiong, C. Wang, Z. Zhang, Y. Qiu, Y. Shi, L. Yin, R. Wang, Melt-infusion-induced electrolyte surface coating stabilized sulfide-based all-solid-state lithium metal batteries. *ACS Nano* **19**, 10912–10921 (2025).

Downloaded from https://www.science.org at Northeastern University on November 13, 2026

18. L. Braks, J. Zhang, A. Forster, P. W. Fritz, J. Oh, M. El-Kazzi, J. W. Choi, A. Coskun, Interfacial stabilization by prelithiated trithiocyanuric acid as an organic additive in sulfide-based all-solid-state lithium metal batteries. *Angew. Chem. Int. Ed. Engl.* **63**, e202408238 (2024).
19. X. Fan, X. Ji, F. Han, J. Yue, J. Chen, L. Chen, T. Deng, J. Jiang, C. Wang, Fluorinated solid electrolyte interphase enables highly reversible solid-state Li metal battery. *Sci. Adv.* **4**, eaau9245 (2018).
20. A. K. Singh, M. Patel, A. P. S. Bais, R. Yadav, A. Bano, Rosy, Role of NaF in attenuating interfacial instability of lithium metal anode: A strategy to modulate SEI for enabling dendrite free lithium metal batteries. *Small* **22**, e12650 (2026).
21. Y. Wang, F. Liu, G. Fan, X. Qiu, J. Liu, Z. Yan, K. Zhang, F. Cheng, J. Chen, Electroless formation of a fluorinated Li/Na hybrid interphase for robust lithium anodes. *J. Am. Chem. Soc.* **143**, 2829–2837 (2021).
22. X. Fan, L. Chen, X. Ji, T. Deng, S. Hou, J. Chen, J. Zheng, F. Wang, J. Jiang, K. Xu, C. Wang, Highly fluorinated interphases enable high-voltage Li-metal batteries. *Chem* **4**, 174–185 (2018).
23. L. Xu, J. Zhang, T. J. Schmidt, M. El Kazzi, Mechanistic insights into soft shorts in all-solid-state lithium metal batteries using a three-electrode and pressure-monitoring cell. *J. Energy Chem.* **117**, 365–375 (2026).
24. D. Cao, T. Ji, Z. Wei, W. Liang, R. Bai, K. S. Burch, M. Geiwitz, H. Zhu, Enhancing lithium stripping efficiency in anode-free solid-state batteries through self-regulated internal pressure. *Nano Lett.* **23**, 9392–9398 (2023).
25. W. Fan, W. Wang, Q. Xie, X. He, H. Li, J. Zhao, J. Nan, A sodium bis(fluorosulfonyl)imide (NaFSI)-based multifunctional electrolyte stabilizes the performance of $NaNi_{1/3}Fe_{1/3}Mn_{1/3}O_2$/hard carbon sodium-ion batteries. *Chem. Eur. J.* **30**, e202401321 (2024).
26. M. Liu, J. J. Hong, E. Sebti, K. Zhou, S. Wang, S. Feng, T. Pennebaker, Z. Hui, Q. Miao, E. Lu, N. Harpak, S. Yu, J. Zhou, J. W. Oh, M. S. Song, J. Luo, R. J. Clément, P. Liu, Surface molecular engineering to enable processing of sulfide solid electrolytes in humid ambient air. *Nat. Commun.* **16**, 213 (2025).
27. N. Riphaus, B. Stiaszny, H. Beyer, S. Indris, H. A. Gasteiger, S. J. Sedlmaier, Understanding chemical stability issues between different solid electrolytes in all-solid-state batteries. *J. Electrochem. Soc.* **166**, A975–A983 (2019).
28. J. Lee, Y. Lee, J. Lee, S. M. Lee, J. H. Choi, H. Kim, M. S. Kwon, K. Kang, K. T. Lee, N. S. Choi, Ultraconcentrated sodium bis(fluorosulfonyl)imide-based electrolytes for high-performance sodium metal batteries. *ACS Appl. Mater. Interfaces* **9**, 3723–3732 (2017).
29. A. Lahiri, M. Olschewski, R. Gustus, N. Borisenko, F. Endres, Surface modification of battery electrodes via electroless deposition with improved performance for Na-ion batteries. *Phys. Chem. Chem. Phys.* **18**, 14782–14786 (2016).
30. L. Peng, T. Lei, S. Cheng, J. Xie, Synergistic fluorine–nitrogen interfaces enabling stable high-voltage sulfide-based all-solid-state lithium metal batteries. *Nano Res.* **18**, 94907614 (2025).
31. J. Oh, S. H. Choi, J. Y. Kim, J. Lee, T. Lee, N. Lee, T. Lee, Y. Sohn, W. J. Chung, K. Y. Bae, S. Son, J. W. Choi, Anode-less all-solid-state batteries operating at room temperature and low pressure. *Adv. Energy Mater.* **13**, 2301508 (2023).
32. Y. Wang, Y. Liu, M. Nguyen, J. Cho, N. Katyal, B. S. Vishnugopi, H. Hao, R. Fang, N. Wu, P. Liu, P. P. Mukherjee, J. Nanda, G. Henkelman, J. Watt, D. Mitlin, Stable anode-free all-solid-state lithium battery through tuned metal wetting on the copper current collector. *Adv. Mater.* **35**, e2206762 (2023).
33. J. Lee, S. H. Choi, G. Im, K. J. Lee, T. Lee, J. Oh, N. Lee, H. Kim, Y. Kim, S. Lee, J. W. Choi, Room-temperature anode-less all-solid-state batteries via the conversion reaction of metal fluorides. *Adv. Mater.* **34**, e2203580 (2022).
34. Y. Sohn, J. Oh, J. Lee, H. Kim, I. Hwang, G. Noh, T. Lee, J. Y. Kim, K. Y. Bae, T. Lee, N. Lee, W. J. Chung, J. W. Choi, Dual-seed strategy for high-performance anode-less all-solid-state batteries. *Adv. Mater.* **36**, e2407443 (2024).
35. J. Oh, Y. Sohn, J. W. Choi, High-performance anode-less all-solid-state batteries enabled by multisite nucleation and an elastic network. *EES Batteries* **1**, 566–575 (2025).
36. Y. Wang, V. Raj, K. G. Naik, B. S. Vishnugopi, J. Cho, M. Nguyen, E. A. Recker, Y. Su, H. Celio, A. Dolocan, Z. A. Page, J. Watt, G. Henkelman, Q. H. Tu, P. P. Mukherjee, D. Mitlin, Control of two solid electrolyte interphases at the negative electrode of an anode-free all solid-state battery based on argyrodite electrolyte. *Adv. Mater.* **37**, e2410948 (2025).
37. J. Kim, S. Lee, J. Kim, J. Park, H. Lee, J. Kwon, S. Sun, J. Choi, U. Paik, T. Song, Regulating Li electrodeposition by constructing Cu–Sn nanotube thin layer for reliable and robust anode-free all-solid-state batteries. *Carbon Energy* **6**, e610 (2024).
38. J. H. Lee, S.-H. Oh, H. Yim, H.-J. Lee, E. Kwon, S. Yu, J. S. Kim, J. Song, J. Koo, J. Cho, S. H. Kim, A. Ryu, S. H. Choi, Y. Kim, G. Im, J.-W. Choi, S.-H. Yu, Interfacial stabilization strategy via In-doped Ag metal coating enables a high cycle life of anode-free solid-state Li batteries. *Energy Storage Mater.* **69**, 103398 (2024).
39. J. Oh, T. Lee, N. Lee, Y. Sohn, J. Y. Kim, K. Y. Bae, S. H. Choi, J. W. Choi, Kinetically engineered lithiophilic dual-metal layers for dendrite-free, high-energy anode-less all-solid-state batteries. *Battery Energy* **4**, e70038 (2025).
40. X. Sun, D. Cao, Y. Wang, T. Ji, W. Liang, H. Zhu, All-solid-state Li–S batteries enhanced by interface stabilization and reaction kinetics promotion through 2D transition metal sulfides. *Adv. Mater. Interfaces* **9**, 2200539 (2022).

Acknowledgments: We acknowledge M. Geiwitz and K. S. Burch for silver deposition on the SS foil. **Funding:** This work was supported by the Office of Science of the US Department of Energy under award number DE-SC0024528 and the US National Science Foundation under award number 2047460. **Author contributions:** H.Z. directed the project. H.Z. and J.W. designed the experiments. J.W. performed the electrochemical characterizations. D.L. performed the LiFSI reference measurement. M.C., X.G., and H.W. helped with XPS and XRD measurements. M.C. and J.W. analyzed the XPS data. M.Y. helped with schematic drawing. J.W. wrote the manuscript. All the authors contributed to the discussion of the manuscript. **Competing interests:** H.Z. and J.W. are inventors on US provisional patent application no. 63/967,106, filed by Northeastern University on 23 January 2026, related to this work. The application is now pending. The authors declare that they have no other competing interests. **Data, code, and materials availability:** All data and code needed to evaluate and reproduce the results in the paper are present in the paper and/or the Supplementary Materials.

Submitted 28 July 2026
Accepted 1 October 2026
Published 13 November 2026
10.1126/sciadv.ael0210

Downloaded from https://www.science.org at Northeastern University on November 13, 2026

ScienceAdvances

Time-evolved hetero-alkali interphases enable long-life sulfide-based anode-free solid-state batteries

Jiwei Wang, Man Chen, Mengting Ye, Xiaolin Guo, Dehang Li, Hui Wang, and Hongli Zhu

Sci. Adv. **12** (46), eael0210. DOI: 10.1126/sciadv.ael0210

View the article online
https://www.science.org/doi/10.1126/sciadv.ael0210
Permissions
https://www.science.org/help/reprints-and-permissions

Downloaded from https://www.science.org at Northeastern University on November 13, 2026

Use of this article is subject to the Terms of service

Science Advances (ISSN 2375-2548) is published by the American Association for the Advancement of Science. 1200 New York Avenue NW, Washington, DC 20005. The title *Science Advances* is a registered trademark of AAAS.

Copyright © 2026 The Authors, some rights reserved; exclusive licensee American Association for the Advancement of Science. No claim to original U.S. Government Works. Distributed under a Creative Commons Attribution NonCommercial License 4.0 (CC BY-NC).